Photoacoustic Imaging of Mesenchymal Stem Cells in Living Mice *via* Silica-Coated Gold Nanorods

Jesse V. Jokerst,[†] Mridhula Thangaraj,[†] Paul J. Kempen, Robert Sinclair, and Sanjiv S. Gambhir[†,‡,*]

[†]Molecular Imaging Program at Stanford (MIPS), Department of Radiology, 318 Campus Drive, Stanford University, Stanford, California 94305-5427, United States, and [‡]Bioengineering, Materials Science & Engineering, Bio-X, Stanford University, Stanford, California 94305, United States

The promises of stem cell therapy (SCT) for musculoskeletal disease such as muscular dystrophy including regeneration of myofibers have been hampered by poor survival of implanted cells.[1−7] A variety of stem cell types have been examined including satellite cells[8] and mesenchymal stem cells (MSCs).[9] MSCs have had few adverse events with the generation of muscle cells.[9−13]

Specific limitations to stem cell therapy (SCT) include cell death, contamination by undifferentiated cells, and cell delivery to untargeted areas.[14] In one of the first human examples of SCT, cells were mis-injected in 50% of patients.[15,16] In that study, cell imaging during injection could not be performed and the poor injection rates were not identified until postprocedure magnetic resonance imaging (MRI) analysis. Although local delivery improves accuracy, there is no way to image and quantitate the number of cells accumulating at the target site in real time. Indeed, it is currently unclear whether the lack of response observed in some SCT is due to poor biology or poor graft delivery.

Imaging is a fundamental tool to improve SCT and can assist with proper delivery of cells and also monitors the short-term and long-term fate of delivered cells.[17] Such imaging is critical to determine the location and quantity of cells during the transplant event, but also the quantity and redistribution during tissue repair. There are two main approaches to stem cell imaging: (1) labeling with a reporter gene or (2) labeling with an exogenous contrast agent. Reporter genes for positron emission tomography (PET) and optical imaging are quantitative and offer content on cell proliferation, but are difficult to envision clinically due to depth limitation (optical) and the need for alteration of the stem cell machinery.

ABSTRACT
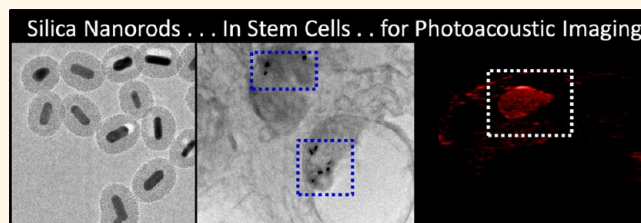
Improved imaging modalities are critically needed for optimizing stem cell therapy. Techniques with real-time content to guide and quantitate cell implantation are especially important in applications such as musculoskeletal regenerative medicine. Here, we report the use of silica-coated gold nanorods as a contrast agent for photoacoustic imaging and quantitation of mesenchymal stem cells in rodent muscle tissue. The silica coating increased the uptake of gold into the cell more than 5-fold, yet no toxicity or proliferation changes were observed in cells loaded with this contrast agent. Pluripotency of the cells was retained, and secretome analysis indicated that only IL-6 was disregulated more than 2-fold from a pool of 26 cytokines. The low background of the technique allowed imaging of down to 100 000 cells *in vivo*. The spatial resolution is 340 μm, and the temporal resolution is 0.2 s, which is at least an order of magnitude below existing cell imaging approaches. This approach has significant advantages over traditional cell imaging techniques like positron emission tomography and magnetic resonance imaging including real time monitoring of stem cell therapy.

KEYWORDS: stem cell therapy · stem cell tracking · photoacoustic imaging · gold nanorod · silica gold nanorod · cell tracking · ultrasound

Alternatively, iron oxide nanoparticles are used for cell imaging with MRI. MRI has excellent resolution, soft tissue contrast, and detection limits (10−20 cells/voxel).[15,17−20] MRI cell tracking was reported nearly a decade ago and is currently capable of single cell imaging.[21,22] Unfortunately, both MRI and PET have temporal resolution of minutes, which precludes them from use during the cellular implantation event.

One alternative approach to these established techniques is photoacoustic (PA) imaging. In photoacoustic imaging (PAI), ultrasound waves are generated *via* a pressure
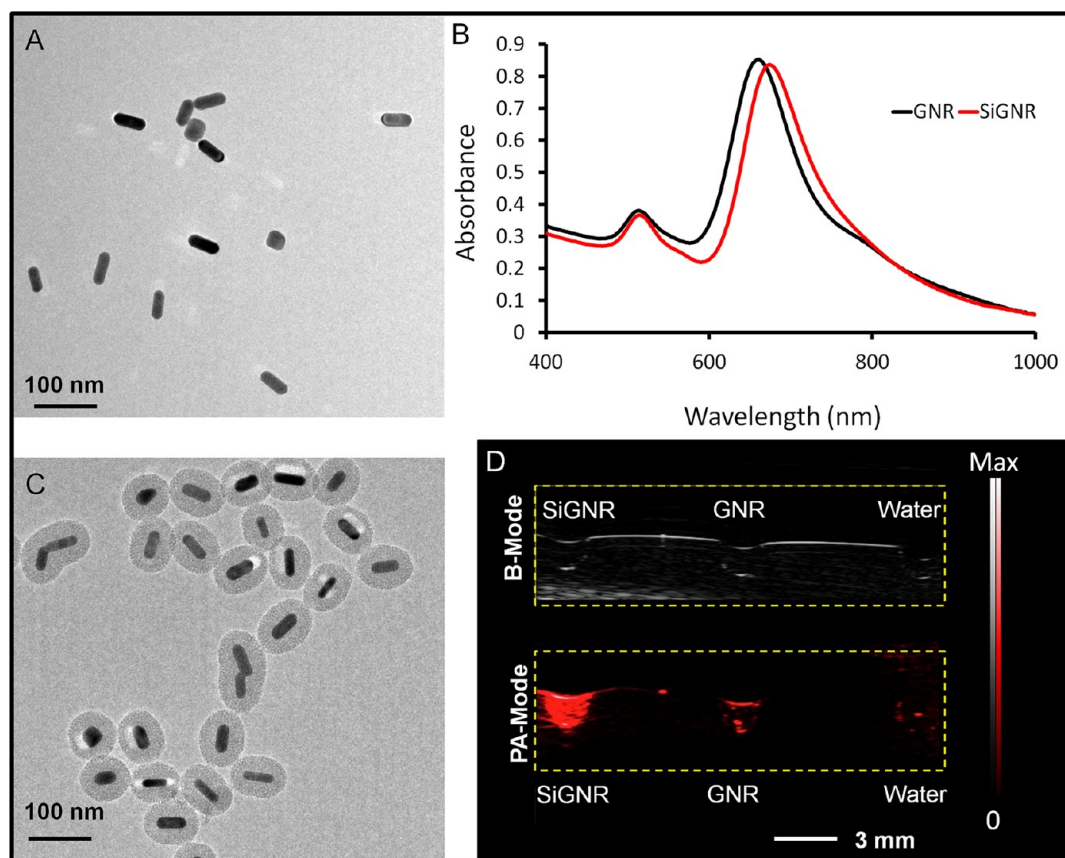
Figure 1. Characterization of SiGNR contrast agent. TEM images of GNRs (A) and SiGNRs (C) were obtained and the materials were studied by absorption spectroscopy at 1:30 dilution of stock solution ($\sim$5 nM) in water. A slight red shift was noted for the silica-coated agents (B). (D) The backscatter (B-mode) and PA signals were studied and the addition of the silica coat increased the PA signal 4-fold. Panels A and C show some imaging artifacts (white) from heterogeneity in nanoparticle size when imaged in a finite focal depth. This is not indicative of an impurity or other species.

difference induced by the rapid heating from a nanosecond light pulse incident on the sample.[23−30] PAI may use either endogenous contrast such as oxy- and deoxy-hemoglobin[31] or exogenous contrast agents such as small molecules,[32] carbon nanotubes,[28,33] or gold nanorods (GNRs).[34,35] PAI is used tangentially with normal backscatter mode (B-mode) ultrasound. It is quantitative, noninvasive, and has short scan times. It is an ideal tool to use for stem cell implantation because B-mode ultrasound will already be used to localize the delivery catheter near the diseased site. PAI can quantitate the implanted cells in real time to confirm that an adequate number of cells reach the treatment site.

In this report, we use silica-coated GNRs (SiGNRs) as a PA contrast agent to label MSCs and image them in the musculature of living mice. Cellular uptake of the contrast agent is facilitated by the silica coat, which also increases the PA signal of the GNRs.[35−37] We measured the effect of the SiGNRs on MSC viability, proliferation, differentiation, and cytokine expression. We imaged and quantitated MSCs in agarose phantoms, and finally injected labeled MSCs into the muscle of living mice to estimate *in vivo* detection limits.

RESULTS

The GNRs and SiGNRs were characterized *via* TEM and absorbance spectroscopy (Figure 1). The GNRs had a peak resonance at 665 nm with average dimensions of 42.17 $\pm$ 5.11 nm by 14.90 $\pm$ 0.58 nm as measured by TEM and ImageJ analysis (Figure 1A). After silica coating (Figure 1B), the dimensions increased to 82.99 $\pm$ 3.86 by 64.20 $\pm$ 3.48 nm width with an additional 11 nm in red-shift of the plasmon resonance to 676 nm (Figure 1C). This 20 nm shell thickness was previously reported to be optimal for PA imaging.[35] DLS indicated that the GNRs had a charge of 14.7 mV and the SiGNRs were 7.8 mV in 1:1 PBS/water.[38] The PA signal of GNRs and SiGNRs at 1.4 nM was also calculated and the silica coating produced a 4-fold increase in PA signal (Figure 1D). Previous reports suggest that silica coating provides a 3-fold increase in PA signal.[35] The 4-fold increase seen here is likely due to a closer matching of the SiGNR peak (676 nm) with the excitation pulse (680 nm) relative to the uncoated GNRs (665 nm).

The PA scanner consisted of three separate components including a light-tight imaging chamber, an excitation source, and a PC-based processing console (Supporting Information, Figures S.1 and S.2). The
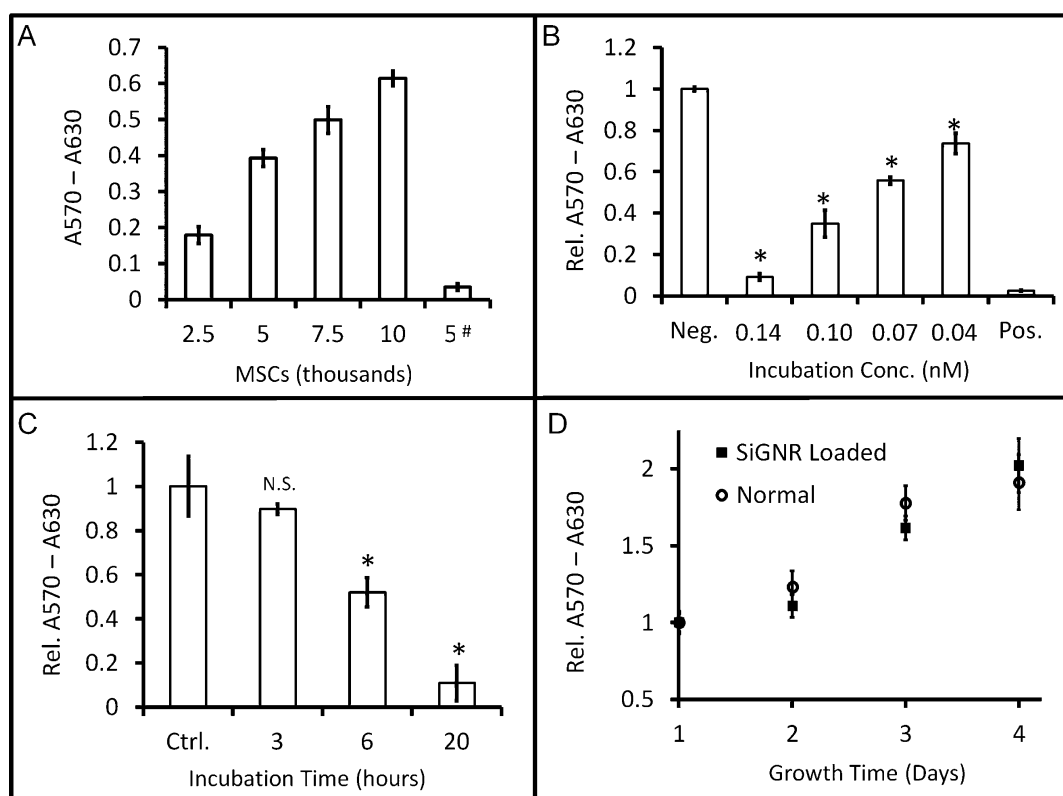
Figure 2. Toxicity and proliferation of SiGNR-labled MSCs. (A) The capacity of the MTT assay to count cells was confirmed with increasing numbers of plated MSCs ("#" indicates cytotoxic positive control; 0.25 mg/mL CTAB). **(B)** Increasing concentrations of SiGNRs show increasing toxicity to 10 000 MSCs after overnight (∼20 h) incubation with SiGNRs. **(C)** The incubation time of one concentration (0.07 nM) was further optimized with 3, 6, and 20 h of incubation. "Ctrl." in panel C indicates no SiGNRs. Incubation at 3 h at this concentration produced an insignificant ($p > 0.05$) decrease in cell metabolism. **(D)** To study the impact SiGNRs have on MSC growth proliferation, MSCs both loaded and unloaded with SiGNRs were serially monitored. There was no significant change to their growth as probed by MTT assay. Both unlabeled and SiGNR-labeled MSCs showed a doubling time of three days. In panels A−C, error bars represent the standard deviation of three replicate experiments. Error bars in panel D represent standard deviation of six replicate wells.

imaging conditions (gain, power, and dynamic range) of the PA instrument for this contrast agent were empirically optimized. For additional details of these descriptors, please see the caption of Supporting Information, Figure S.3. The laser power was monitored with an external power meter as well as internal power sampling. At 680 nm, the average power detected 1 cm away from the transducer was 9.5 mJ (6.9−12.9 mJ) with root-mean-square variation of 10.1% for 500 pulses. Supporting Information, Figure S.3 presents an experiment in which other parameters were sequentially modulated and the resulting signal from the contrast agent was plotted along with the signal-to-background ratio. Optimal conditions were achieved with a gain of 50 dB, 80% power, a persistence of four frames (no persistence was used for real time imaging), and 20 dB of dynamic range. These conditions were used for the remainder of the experiments. The spatial resolution was probed by imaging a test pattern printed on transparency film. Spacing of 340 μm was easily resolved while spacing of 58 μm could not be resolved (Supporting Information, Figure S.4). There was a linear relationship ($R^2 > 0.99$) between concentration (up to 0.7 nM) and PA signal of the SiGNRs in an

agarose phantom with a LOD of 0.03 nM SiGNRs (Supporting Information, Figure S.5A,B). No decrease in PA signal intensity was observed for the SiGNRs over 60 days.

The capacity of SiGNRs to label MSCs was studied next. Previously, silica has facilitated endocytosis into a variety of cell types, including MSCs.[39,40] To choose the appropriate starting concentration and incubation time of the SiGNRs, we used the MTT cell toxicity assays and centered the study near 0.05 nM SiGNRs, which has previously shown efficacy for cellular labeling with gold core/silica shell nanoparticles (Figure 2).[41] Both SiGNR concentration (Figure 2B) and the incubation time (Figure 2C) were studied. The results indicate that 0.07 nM of SiGNRs (1.5×10^6 SiGNRs/MSC) at 3 h of incubation time gave no statistically significant change in MSC metabolic activity relative to the negative control ($p > 0.05$). To confirm SiGNR endocytosis, TEM images of fixed cells were acquired, and accumulation of SiGNRs inside MSC vesicles was noted (Figure 3 and Supporting Information, Figure S.6). The silica coat was not entirely clear because the electron density of silica is approximately the same as the 400 nm section of resin.
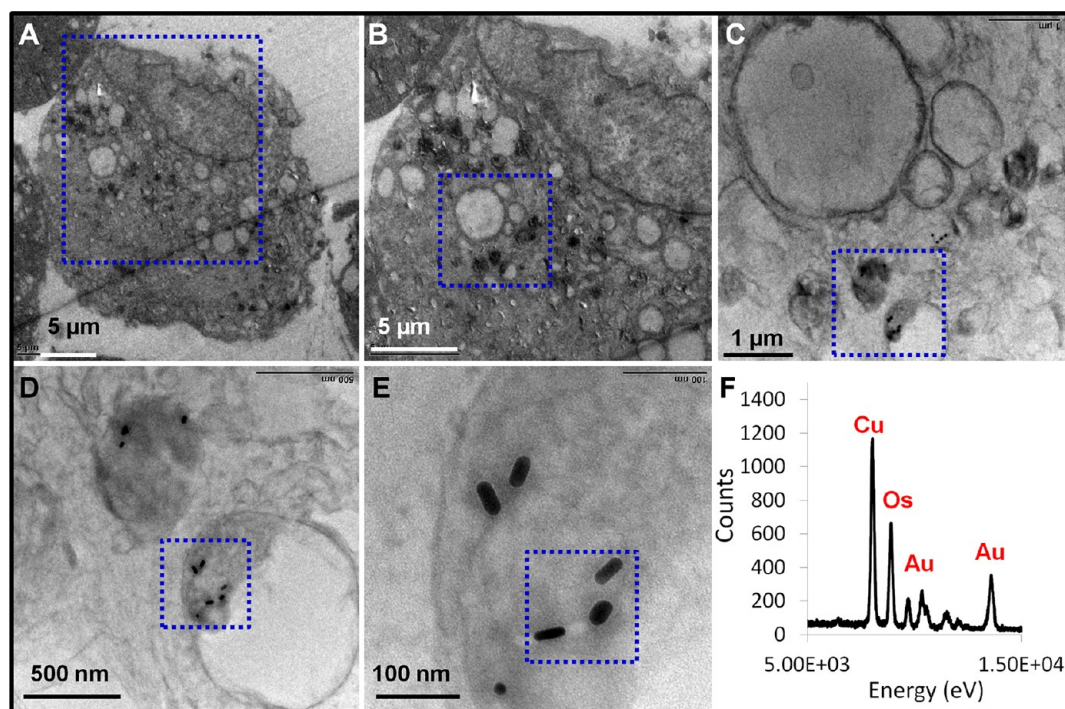
Figure 3. Confirmation of SiGNRs inside MSCs. (A–E) TEM images of MSCs loaded with SiGNRs were collected at increasing magnifications. The dashed, colored inset in panels A–E correspond to the sequential, higher magnification image in the following panel. Panel E clearly shows nanorods inside a MSC vesicle. Panel F is a portion of the EDS spectra acquired on panel E (dashed inset) that confirms the presence of gold. The presence of Cu is from the Formvar-coated TEM grid and Os is from the OsO_4 stain. The silica coat is not highly visible because the electron density of silica is nearly equivalent to the stained cells. See additional example in Supporting Information, Figure S.6.

The capacity of GNR- and SiGNR-labeled MSCs to generate a PA signal was studied relative to nanoparticle free-MSCs, all at 50 000 cells (in 15 μL) in an agarose phantom (Supporting Information, Figure S.7). Maximum intensity projections were created to analyze the data with ROI analysis. A 2.8-fold increase was measured for the GNR-labeled MSCs relative to unlabeled MSCs. The signal of GNR-MSCs was 7.6-fold lower than the same number of MSCs with SiGNRs (Supporting Information, Figure S.7C). Theoretically, this increase should have been 20-fold (5 times more contrast with 4 times more signal). This lower observed signal is likely due to optical attenuation and scatter that occurs inside the MSC. The effect of incubation time on PA signal of MSCs was also measured for the 3, 6, and 20 h time points at 0.07 nM. The 6 h time point had the same ($p = 0.33$) PA intensity as the 3 h incubation sample, but the 20 h sample was reduced. The PA signal of the 20 h sample was 34% of the 3 h sample. To determine the *ex vivo* LOD, we immobilized decreasing numbers of SiGNR-loaded MSCs into a phantom and collected PA images. The LOD above the water blank was 5000 cells (Supporting Information, Figure S.7B).

ICP analysis determined the amount of gold loaded into the cells. First, an increasing number of GNRs and SiGNRs were analyzed for their gold content and that signal was plotted in Supporting Information,

Figure S.8A. This calibration plot was used with the gold content of dissolved MSCs to determine the number of SiGNRs present in the total sample as well as the quantity on a per-cell basis. We calculated 102 000 $\pm$ 1000 SiGNRs per MSC; the gold signal from SiGNR-loaded MSCs was 5-fold higher than that from GNR-loaded MSCs (Supporting Information, Figure S.8C).

We performed additional studies to determine whether the SiGNRs altered the normal behavior of MSCs beyond gross toxicity assays like the MTT metabolic tests. First, to determine whether this loading changes the normal proliferation of MSCs, 3000 MSCs with and without SiGNR loading were seeded in a 96 well plate and monitored sequentially with MTT. There was no significant ($p = 0.35$) difference between the growth of the two cell populations (Figure 2D). The doubling time for both populations was 3 days.

Next, we used differentiation reagents to determine whether the SiGNRs impacted the pluripotency of the MSCs.[42] This work sought to answer two questions: (1) Can SiGNR-loaded MSCs still differentiate?[43] and (2) Does the presence of SiGNRs induce any unintended differentiation? We were especially concerned that the SiGNRs might unintentionally transform MSCs into osteogenic cells as silicon-based structures have previously been show to induce such differentiation.[44] Fortunately, SiGNR-loaded cells were still easily transformed
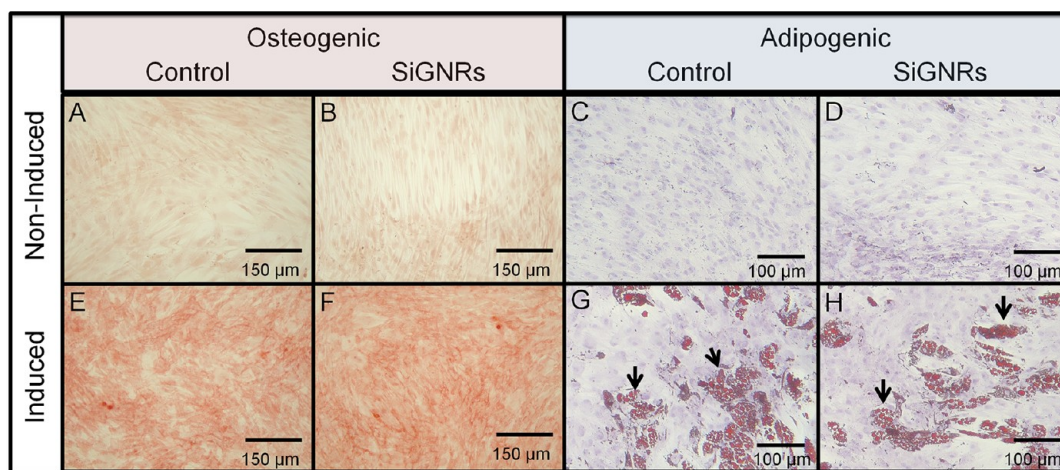
Figure 4. Histology images confirm that the osteogenic and adipogenic differentiation capacity of MSCs is unchanged by the presence of SiGNRs. Cells in images on the top row are noninduced controls, while the bottom row was cultured in either osteogenic (left) or adipogenic (right) media. The experiments presented in panels B, F, D, and H were performed on cells loaded with SiGNRs before plating. Panels A, E, C, and G are unloaded control cells. Both loaded and unloaded cells show increased mineral deposition as determined by Alizarin Red S staining in the osteogenic experiments (red color; E, F). Differentiation into adipocytes is similarly unaffected by the presence of the nanoparticles. Black arrows in G and H highlight lipid vacuoles stained by Oil Red O. Importantly, not only is differentiation capacity retained, but the presence of SiGNRs does not induce unintended differentiation (B and D) (see Supporting Information, Figure S.9 for white light photographs of the cell culture plates).

into osteogenic and adipogenic cell lines (Figure 4). There was 5-fold more osteogenic signal (as determined by A402) in the induced (Figure 4F) cells than noninduced cells (Figure 4B). Adipogenic induction produced many lipid-containing vacuoles in both the control (Figure 4G) and SiGNR containing cells (Figure 4H) (see photographs of the culture plates in Supporting Information, Figure S.9).

A final study analyzed the secretome of SiGNR-loaded and control MSCs.[45] Of the 31 analyzed proteins, 26 had levels in cell culture media that were measurable by the bead-based Luminex assay (Supporting Information, Table S.1).[46] We compared the levels in the labeled MSCs to unlabeled MSCs and found that only interleukin-6 (IL-6) had expression patterns increased or decreased more than 2-fold.

The utility of SiGNRs in living systems was first probed by implanting decreasing concentrations of SiGNRs (80 μL of 0.7, 0.35, and 0.175 nM in 50% matrigel) subcutaneously and performing PA imaging. The LOD for the SiGNR contrast agent *in vivo* (subcutaneous) was 0.05 nM and linear at $R^2 = 0.93$ (Supporting Information, Figure S.5B,D). The next step was to inject SiGNR-labeled MSCs. Figure 6 presents representative sequences of intramuscular cell implantation (Figure 6, right) including positive (Figure 6, left) and negative controls (Figure 6, middle). Images of hind limb muscle and images, during, and after injection are shown. For video of real-time injection of the SiGNR-labeled MSCs presented in the right of Figure 6, please see Supporting Information, Video 1, with speed increased 8-fold and Video 2 in real time. The positive control is 3 nM SiGNRs only, the negative control is PBS, and the cell implantation is 800 000 cells. Importantly,
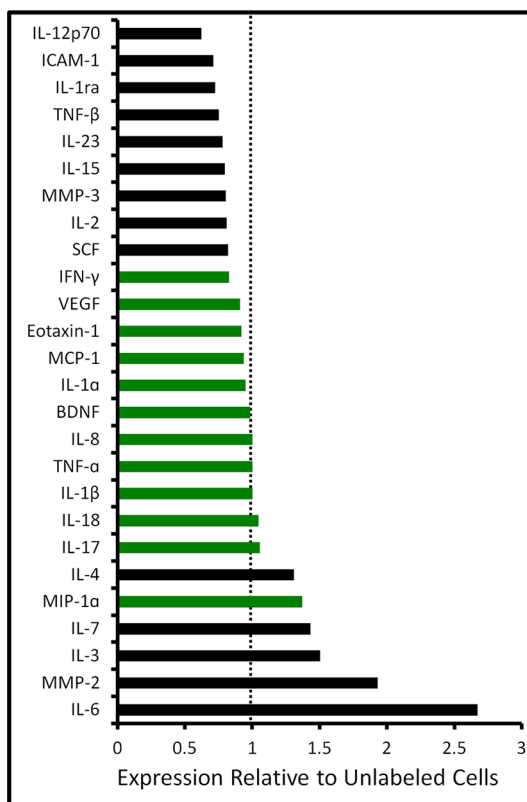

Figure 5. Secretome analysis of labeled cells. The change in secretome cytokine expression levels is shown for 26 different proteins. Cell culture media from SiGNR-loaded MSCs and control MSCs was analyzed for these proteins. The concentration of protein in SiGNR-loaded cells was divided by the concentration in controls cells to produce the metric above. Except for IL-6, no protein had a concentration that changed more than 200% (1-fold change). Black bars indicate a statistically significant ($p < 0.05$) change in expression; green bars indicate a *p*-value above 0.05. Please see Supporting Information, Table S.1 for actual values and additional statistical content.
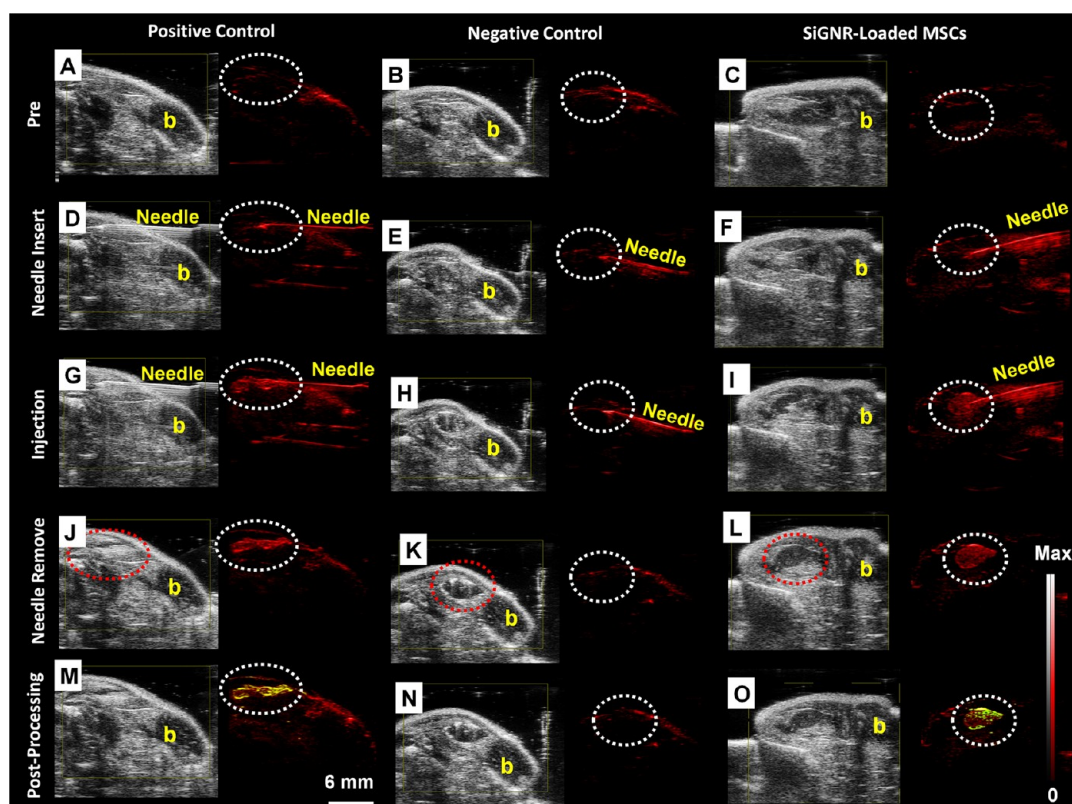
Figure 6. *In vivo* positive and negative controls; labeled MSC injection. This figure presents both B-mode (gray scale) and PA (red) images of the intramuscular injection of a positive control (0.7 nM SiGNRs; left), negative control (0 nM SiGNRs (no cells); middle), and 800 000 SiGNR-labeled MSCs (right) all in 50% matrigel/PBS into hind limb muscle of an athymic mouse. Imaging sequence is as follows: preinjection (A, B, C); needle insertion and position (D, E, F); postinjection (G, H, I); needle removal and final imaging (J, K, L), and contrast enhancement to illustrate increased signal (M, N, O). Pixels increased relative to preinjection image are coded yellow. Note significant signal increase in M and O at injection site relative to A and C (dashed circles highlight injection site). Also, note low signal in negative control (N). Scale bar in M and intensity scale in L/O applies to all images. The "b" in all panels indicates bone and the red dashed circle in J, K, L indicates that the injection bolus can also be seen with B-mode ultrasound. Real time injection imaging of cells between panels F and I may be seen in Supporting Information, Video 1 (at 8× speed) and in real time (Supporting Information, Movie 2).

the B-mode image shows the implant in all three examples (Figure 6J, K, and L). The red dashed circle highlights the injection site. For Figure 6K, there is clearly an i.m. bolus injection, but no PA signal. In contrast, Figure 6L with SiGNR-MSCs shows a bolus and PA signal. Spectral analysis of the therapy site was performed before and after injection (Figure 7A).

The difference pre- and postinjection at the injection site was 670% increase for positive control; no increase in PA signal was observed for the negative (vehicle) control. Decreasing numbers of SiGNR-labeled MSCs (8×10^5 to 1×10^5) were delivered into a mouse hind limb muscle in three replicate mice at each different cell number (Figure 7B and Supporting Information, Figure S.10) The lowest value imaged was 100 000 cells and the calculated *in vivo* LOD of MSCs in mouse hind limb muscle is 90 000 cells. One animal with 100 000 cells was monitored longitudinally and a PA image recorded daily. The implanted cell bolus could be monitored for 4 days after injection (see Supporting Information, Figure S.10).

To validate the imaging data we performed histological analysis in which treated muscle tissue was removed after injection (cells in this example were labeled prior to injection with a green cell tracking fluorophore), fixed, and stained with hematoxylin and eosin. This sample was first placed in a fluorescence imaging chamber using green fluorescent protein filter cubes. Intense green fluorescence is seen corresponding to the green cell tracking dye in the MSCs (Supporting Information, Figure S.11) The resulting histology slide shows very clear morphological differences between skeletal muscle (Figure 7C; right) and the delivered cells (Figure 7C; left). The fluorescence of the cell tracking dye is obvious when an adjacent slice is imaged with fluorescence (Figure 7D). Although there was some damage during sample preparation causing the delivered cells to lose adherence to the muscle tissue, this confirms that the increase in imaging signal is due to cells. Interestingly, at 40× magnification, dark spots are present in MSCs, likely due to SiGNRs (Figure 7E).

DISCUSSION

SiGNRs were used as a photoacoustic contrast agent to image MSCs implanted into rodent muscle. The silica
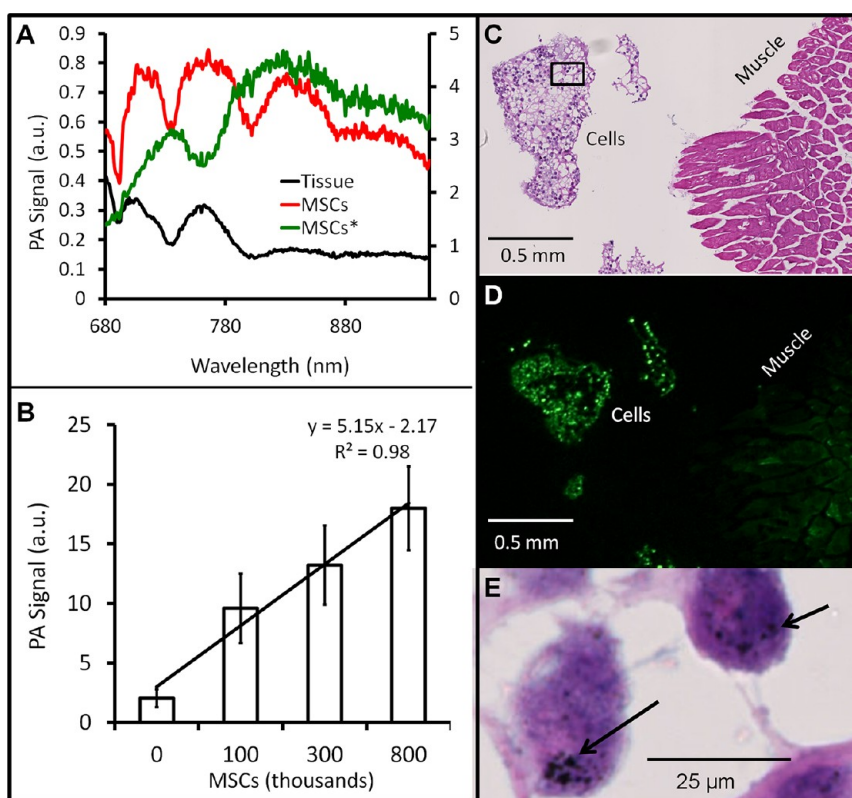
Figure 7. Validation of imaging data. (A) Spectral analysis of tissue and 800 000 MSCs after i.m. injection. Also shown in green is the normalized spectral analysis of the MSCs *in vivo*. A broad increase in PA signal is seen, which may be due to aggregation and resonance coupling of the contrast (see 7E and Supporting Information, Figure S.6). This normalized spectrum is more red-shifted *versus* SiGNRs imaged in a phantom (Supporting Information, Figure S.3D). That experiment suggested an intensity maximum near the absorbance peak shown in Figure 1. (B) The average signal for decreasing numbers of cells and as well as the negative control indicate that the calculated estimate for limit of detection is 90 000 cells. A sampling of 100 000 cells was easily imaged above background injection. Error bars represent the standard error of the background-corrected signal for each group of mice. (C) H&E staining of muscle tissue (right) with adjacent MSCs (left). (D) The fluorescence of a cell tracking dye (green) from an adjacent section illustrates higher signal for MSCs than muscle tissue. (E) Higher magnification of MSCs shows SiGNRs (black) inside the cells (black arrows).

coat played two important roles—it enhanced the photoacoustic signal of the GNRs[47] (Figure 1) and increased uptake of the GNRs into the cell (Supporting Information, Figure S.8). TEM evidence suggested that the SiGNRs were endocytosed into vesicles inside the MSCs (Figure 3 and Supporting Information, Figure S.6). Optimal conditions (3 h incubation at 0.07 nM) were found such that PA signal remained high, but with no negative impact on cell metabolism or proliferation (Figures 2, 4, and 5). This approach allows real-time (5 frames per second) PA imaging with the B-mode ultrasound image offering clear anatomic features and the photoacoustic data showing cell specific content at submm resolution.

Very good detection limits for both the contrast alone (0.03 nM) and MSCs (5000 *ex vivo*; 90 000 *in vivo*) were measured and thus the sensitivity of this approach is suitable for imaging MSCs *in vivo*. Furthermore, the injection procedure (25 gauge catheter) caused very little trauma resulting in background photoacoustic signal (Figure 6H,K,N). It is important to note that the number of cells used here is more than 2 orders of magnitude below what would be delivered

clinically, and complements nicely the existing ultrasound infrastructure.[48]

Previous reports have shown that surface charge, polymer coatings, and incubation concentration can affect the loading level of GNRs into cancer cell lines including MBT2,[49] HeLa,[50] and HT29 cells.[51] Values in these experiments range from 50 to 150 000 nanorods per cell.[49−51] This work with SiGNRs shows that a very high amount of contrast can be loaded into these cells (101 000 $\pm$ 1000 SiGNRs/MSC by ICP). For 30 μm diameter MSCs, this translates into 0.005% of the cell volume being occupied by SiGNRs or 12 nM. While this value is much higher than the concentration shown to induce toxicity (Figure 2), this *in vivo* concentration is in vacuoles that likely prevent toxicity. Nevertheless, proliferation, and metabolic screens indicated these MSCs behaved as nonlabeled MSCs (Figure 2). The pluripotency of the MSCs is retained as illustrated for osteogenic and adipogenic differentiation (Figure 4). Furthermore, there is no unintended differentiation, which is a concern since nanoparticles can sometimes give rise to spontaneous osteogenesis.[52,53] More importantly, the relatively stable secretome suggests

most cellular pathways are unaffected by SiGNRs and that any paracrine effects of MSC therapy will remain available to damaged tissue.[54]

However, there are some important considerations to measuring SiGNR-labeled cells. Challenges inherent to PA imaging include light scatter, inaccuracies in reconstructions, frequency/signal changes due to volume modifications, tissue background, and attenuation of the excitation source. The signal may be especially reduced at deeper implant sites, even though some reports show PA depth penetration of several centimeters.[23,55] Although suitable for imaging cells in muscle tissue, applications in deeper areas may require the use of a photoacoustic catheter or endoscope, which are under construction in our lab. Also in preparation are more sophisticated analysis schemes to analyze the images on a pixel-by-pixel basis rather than with ROI analysis. We continuously monitored one treated animal; the cell bolus could be monitored for 4 days after injection (Supporting Information, Figure S.10), but further work is needed to use PAI along for long-term cell tracking due to the limitations mentioned above. In addition, the current generation of tunable lasers do not have extremely tight stability of power output—resolving the stability of laser power is critical to making reproducible photoacoustic measurements since PA signal directly correlates to the intensity of the incident laser pulse. Future work will explore multispectral imaging. In the meantime, we use a feedback loop (Supporting Information, Figure S.1) in which the laser output power is constantly monitored and the resulting output PA signal is normalized to the laser intensity.

Importantly, clinical adaptations of this work could only label a percentage of the cells, leaving the remainder free of contrast. The next generation of this contrast agent may have a larger aspect ratio to induce longer red-shifted resonances.[56] Finally, we will dope Gd^{3+} into the silica shell of the SiGNRs for T1 magnetic resonance imaging[43] to complement the PA mode for long-term monitoring of implanted MSCs with greater depth of penetration. B-mode imaging for visualization of the delivery catheter and the *in vivo* environment is complemented nicely by PA-mode that specifically enhances MSC signal.

CONCLUSION

SiGNRs were used as PA contrast agents to label MSCs. Cells were imaged *ex vivo* in an agarose phantom and *in vivo* after intramuscular injection. Cell detection limits *in vivo* (100 000) were well below clinically relevant numbers. Imaging data was confirmed with histology. Proper cell loading conditions were selected such that metabolism, proliferation, and pluripotency were retained. Secretome analysis indicates that a wide variety of cytokines and chemokines were differentially expressed in the SiGNR-labeled MSCs, but 25 of the 26 proteins had expression levels with changes within one-fold of baseline. These data suggest that the therapeutic benefit of the MSCs will be retained despite the presence of contrast agent and the 0.2 s temporal resolution of the PA imaging technique can offer real time content on cell location and number.

MATERIALS AND METHODS

Reagents. The following reagents were acquired and used as received: cetyltrimethylammonium bromide (CTAB; Sigma Aldrich), gold(III) chloride (Sigma Aldrich), sodium borohydride (Fluka), ascorbic acid (Sigma Aldrich), silver nitrate (Acros), 10 M sodium hydroxide (Sigma Aldrich), tetraethyl orthosilicate (TEOS, Acros), dimethylthiazolyl-diphenyltetrazolium (MTT; Biotium), phosphate buffered saline (PBS, Gibco), SP-DiOC18(3) cell tracking dye (Invitrogen), Oil Red O (Sigma Aldrich), Alizarin Red S (Sigma Aldrich), and agarose (Invitrogen). Millipore water (at 18 MOhm) was used. A Synergy 4 (Biotek) microplate reader was used for cell assays.

Gold Nanorod Synthesis. The GNRs were prepared *via* the seeded-growth mechanism previously described with slight modifications.[56,57] Briefly, gold seed was prepared by the addition of 5 mL of 0.2 M CTAB to 5 mL of 0.005 M gold chloride in a scintillation vial. Then, 0.6 mL of 0.01 M $NaBH_4$ (previously chilled for 10 min in an ice water bath) was quickly added, and the mixture was shaken for 2 min. The growth mixture was prepared with the following: 250 mL of 0.2 M CTAB, 250 mL of 0.001 M $AuCl_3$, and 12 mL of 4 mM $AgNO_3$. This solution was yellow/brown, but became translucent upon the addition of 3.5 mL of 0.0788 M ascorbic acid. Seed (0.6 mL) was then added, and the solution became purple/brownish over 30 min. The GNRs were purified with four rounds of centrifugation and water washing at 16 000 rcf for 20 min and characterized with transmission electron microscopy (TEM), absorption spectroscopy, and dynamic light scattering (DLS; Malvern Zetasizer).

A molar extinction coefficient from the literature of 3.1×10^9 M^{-1} cm^{-1} at the peak resonance was used for GNRs with resonance near 660 nm.[58,59]

Silica Coating. SiGNRs were prepared by diluting stock GNRs to 2.2 nM in water (10 mL total volume) and treating with 100 μL of 0.1 N NaOH to achieve pH of ~10. TEOS (6 μL) was added three times, 30 min apart, and the reaction was allowed to proceed overnight.[60] The next day, SiGNRs were centrifuged at 6000 rcf for 5 min, redissolved in water, and briefly sonicated to resuspend.

Cell Culture. All experiments were done with MSCs between passage number 3 and 12 and used 3−6 replicate wells. Cells and media (including differentiation media) were acquired from Lonza. Unless otherwise noted, cells were plated at 5000 cells/cm^2 of culture plate area and loaded with nanoparticles 2−7 days after plating (~ 80% confluence). Cells were counted after harvest and washing. The total number of cells required was dependent on the end application. We used large T225 flasks (25 mL volume) for the muscle implantation experiments, T75 flasks (10 mL volume) but six well plates (2 mL) for the loading optimization assays. To label MSCs with SiGNRs, we added SiGNRs to the culture flasks at a working concentration between 0.0 and 0.14 nM SiGNRs with incubation from 3 to 20 h. Cells loaded with silica-free GNRs were treated identically to the SiGNRs. Cells were then washed thrice with PBS and removed from the flask with TripLE express (Invitrogen). Toxicity assays were performed by plating 10000 MSCs/well in 96 well plates and loading SiGNRs *in situ*. Proliferation assays

started with a 3000 cells/well with six replicate wells in 96 well plates.

Inductively Coupled Plasma (ICP). We used ICP to determine the amount of SiGNRs in MSCs. There were 50000 MSCs plated in each well of a six-well plate and these were grown to near confluency. Three groups were used: MSCs with SiGNRs, MSCs with regular GNRs, and MSCs with no contrast agent. Cells with contrast agent were loaded with SiGNRs or GNRs with isomolar (0.07 nM) and isovolume (2 mL) conditions along with MSCs with no contrast agent. After 3 h, the media of all wells was removed, and cells were washed three times with room temperature PBS and removed with trypsin. Cells were counted and transferred to 20% aqua regia in water to dissolve the SiGNRs. The samples were placed in a bath sonicator for 20 min to ensure complete dissolution of the cell. Gold ICP standard (Fluka) was used to construct a standard curve. The volume was brought to 5 mL and analyzed for the presence of gold ions with an IRIS Advantage/1000 Radial ICAP spectrometer (Thermo Scientific). Standards were analyzed in duplicate, and cells samples were analyzed in triplicate with nearly 100 000 MSCs analyzed per sample.

Differentiation Experiments. Low passage number (<6) MSCs were used for differentiation experiments. Cells were loaded with SiGNRs as described above and the labeled cells were counted and plated as described below. Stained cells were imaged with a Leica light microscope.

The osteogenic protocol used 35 mm collagen-coated culture plates (World Precision Instruments) and 30 000 cells (loaded and unloaded with SiGNRs) per plate. The next day, standard media was replaced with osteogenic media (Lonza PT-3002). Control cells used standard media, and osteogenic media was supplemented with dexamethasone, ascorbate, and β-glycophophate. The media for both control and labeled cells was changed every 2−3 days. After 24 days, cells were fixed with 70% ethanol on ice for 1 h and then stained with 2% Alizarin Red in water (pH 4.2; freshly filtered) for 7 min followed by water washes until no excess stain was removed. The degree of osteogenesis was quantitated by dissolving the colored complex in 10% acetic acid and measuring A402.

In the adipogenic protocol, 80 000 loaded and unloaded cells were seeded in a 12 well plate and grown for 7 days until they were overconfluent. Cells in the induced population were subjected to three rounds of three-day growth in induction media (Lonza PT-3004) followed by 1−3 intervals in maintenance media. Adipogenic induction media contained recombinant insulin, dexamethasone, indomethacin, 3-isobutyl-1-methyl-xanthine, and gentamicin. Adipogenic maintenance media contained only insulin and gentamicin. Control cells were incubated only in maintenance media. One week after the final round of induction, cells contained a large number of microscopic lipid vacuoles. The MSCs were fixed in 10% formalin for 45 min and washed with water and then 60% isopropyl alcohol. Oil red O was used to stain the adipogenic cells. To prepare this stain, 18 mL of water was added to 27 mL of 3 mg/mL Oil red O in isopropyl alcohol. After 10 min the solution was filtered and added to the fixed cells for 5 min followed by a water wash. Cells were counterstained with hematoxylin for 2 min.

Cytokine Expression. Cells with and without SiGNRs were plated at 20000/cm^2 in a 12-well plate and cultured for 2 days. The media was then exchanged and allowed to stand for 24 h. That media from positive, and the control cells were then removed along with media without cells that had been in the incubator for the same amount of time. Secretome analysis was performed with a bead-based assay (Luminex) by a commercial operator (Rules Based Medicine; Austin, TX).[46] Assays used eight calibration standards per protein and three controls. The antibodies for capture and detection were directed against all isotypes.[61] Every protein was measured with a redundancy of 50 beads.

PA Imaging. Photoacoustic imaging was performed with a LAZR commercial instrument (Visualsonics) equipped with a 21 MHz-centered transducer and described previously.[62] The system uses a flashlamp pumped Q-switched Nd:YAG laser with optical parametric oscillator and second harmonic generator operating at 20 Hz between 680 and 970 nm with a 1 nm step size and a pulse of 4−6 ns. The peak energy is 45 ± 5 mJ at 20 Hz at the source. The spot size is 1 mm × 24 mm, and the full field of view is 14−23 mm wide. Acquisition rate is 5 frames per second. Imaging the SiGNRs was originally done in agarose phantoms. These were prepared by first boiling 1 mg/mL agarose in degassed distilled water and pouring 20 mL of the hot mixture into a 10 cm Petri dish and allowing it to cool briefly. Once sufficient surface tension had been achieved due to cooling ($\sim$ 2−3 min), we added 2.5 cm sections of polyethylene tubing (Intramedic, PE190, outer diameter 1.70 mm), which floated on top of the agarose and served as a mold. After complete cooling, the tube molds were removed to leave an indentation in the cooled gel. These voids were filled with either contrast agents or MSCs (15 μL) mixed with 15 μL of 50% warm 1 mg/mL agarose. The phantom was sealed with a final 2−4 mm of agarose. Typical imaging conditions include 100% power, 50 dB gain, 21 MHz frequency, and 680 nm excitation. The laser output was monitored externally on the animal bed with a Gentec-eo power meter with sensor 1 cm from end of the PA transducer as well as internal power sampling.

Animal Studies. Female nu/nu mice (6−16 weeks old) were used in this study in triplicate at each data point. All animal work was conducted in accordance with the Administrative Panel on Laboratory Animal Care at Stanford University. Prior to imaging, mice were anesthetized with 2% isofluorane in house oxygen at 2 L/min, which was confirmed with tail pinch. MSCs pellets were resuspended in 40 μL of PBS and mixed with an equivalent volume of ice-cold matrigel. This 80-μL cell-containing bolus was loaded into a 0.5 mL insulin syringe (20 μL of dead volume) and allowed to come to room temperature prior to delivery to increase the viscosity of the material. Delivery used the syringe in tandem with a 25 gauge winged infusion set. For histology confirmation, cells were labeled with a lipophilic carbocyanine cell tracing dye (SP-DiOC18(3)) prior to injection. This protocol used a 1 μM working solution for 5 min in the cell culture incubator on adherent cells followed by 15 min in the cold room. Cells were then removed with trypsin for injection.

Histology. Tissue sections were removed and immediately placed in 10% buffered formalin (Fisher) for 2 days and then transferred to 30% sucrose in PBS. Sections were then placed in optimal cutting temperature (OCT) media and froze for 10 s in a bath of isopentane that was immersed in a bath of liquid nitrogen. Tissue sections (6 μm) were sliced and placed on charged slides and imaged with an automated histology slide reading tool (Nanozoomer).

Microscopy. All transmission electron microscopy (TEM) and energy-dispersive X-ray spectroscopy (EDS) was performed with a Tecnai G2 X-Twin (FEI Co.) instrument operating at 200 kV. After loading with SiNPs, MSCs were washed three times with PBS, removed from the flask with tryspin, and washed with media and saline using 5 min of 1000g centrifugation to create the pellet and prepared for TEM as described previously.[63] Briefly, cells were transferred to a 2:1:1 solution of 0.2 M sodium cacodylate buffer/10% glutaraldehyde/8% paraformaldehye (EMSdiasum). Samples were then stored at 4 °C before being stained *en bloc* with osmium tetroxide. After 2 h, samples were rinsed with deionized water and stained with uranyl acetate overnight. Samples were dehydrated in progressively higher concentrations of ethanol in water: 50, 70, 95, and 100%. Samples were further dehydrated using propylene oxide and embedded in Embed 812 epoxy resin (EMSdiasum). Thin sections (500 nm) were cut using a Leica Ultracut S microtome and placed on a 200-mesh bare copper grid (Ted Pella). Fluorescence microscopy was performed with a Leica Confocal System and white light microscopy utilized an Axiovert 25 ster-omicroscope (Zeiss) fitted with a CCD detector and MR Grab software.

Data Analysis. The limit of detection (LOD) was defined as signal detectable three standard deviations above the mean signal of the blank. Images were saved as RGB TIFF files and analyzed with Image J software.[64] In phantoms, PA signal intensity was measured by region of interest (ROI) analysis and signal was defined as the PA-mode contrast generated by the SiGNR inclusion. Background was defined as the PA-mode

ultrasound contrast generated by the agarose gel surrounding the inclusion. In animals, we created contrast enhanced images by subtracting the pre- and postinjection PA images and taking the mean in the ROI. We then performed a dynamic threshold on the image. We used the ROI mean for the lower end and the three times that mean on the upper end. These pixels were then assigned to a green look up table, overlaid with the original postinjection (red) image to illustrate enhanced pixels by making the resulting positive pixels green or yellow (green + red). The animal LOD was determined as above using the mean ROI intensity at the injection site and sham injection. Analysis of secretome data divided the mean value of the SiGNR cells by control cells (no SiGNRs). Statistical analysis of secretome data used a two tailed t test with 49 degrees of freedom ($t = 1.960$) with the assumption that the coefficient of variation applied to both SiGNR and control samples. P-values were calculated from the experimental t values using Microsoft Excel command "T.DIST".

Conflict of Interest: The authors declare no competing financial interest.

Supporting Information Available: Supplementary images (Figures S.1−Figure S.11), table (Table S.1), and two videos. This material is available free of charge *via* the Internet at http://pubs.acs.org.

REFERENCES AND NOTES

1. LaBarge, M. A.; Blau, H. M. Biological Progression from Adult Bone Marrow to Mononucleate Muscle Stem Cell to Multinucleate Muscle Fiber in Response to Injury. *Cell* **2002**, *111*, 589–601.
2. Meregalli, M.; Farini, A.; Parolini, D.; Maciotta, S.; Torrente, Y. Stem Cell Therapies to Treat Muscular Dystrophy: Progress to Date. *BioDrugs* **2010**, *24*, 237–247.
3. Sohn, R. L.; Gussoni, E. Stem Cell Therapy for Muscular Dystrophy. *Expert Opin. Biol. Ther.* **2004**, *4*, 1–9.
4. Corbel, S. Y.; Lee, A.; Yi, L.; Duenas, J.; Brazelton, T. R.; Blau, H. M.; Rossi, F. M. V. Contribution of Hematopoietic Stem Cells to Skeletal Muscle. *Nat. Med.* **2003**, *9*, 1528–1532.
5. Torrente, Y.; Belicchi, M.; Sampaolesi, M.; Pisati, F.; Meregalli, M.; D Antona, G.; Tonlorenzi, R.; Porretti, L.; Gavina, M.; Mamchaoui, K. Human Circulating Ac13+ Stem Cells Restore Dystrophin Expression and Ameliorate Function in Dystrophic Skeletal Muscle. *J. Clin. Invest.* **2004**, *114*, 182–195.
6. Price, F.; Kuroda, K.; Rudnicki, M. Stem Cell Based Therapies to Treat Muscular Dystrophy. *Biochim. Biophys. Acta* **2007**, *1772*, 272–283.
7. Shabbir, A.; Zisa, D.; Leiker, M.; Johnston, C.; Lin, H.; Lee, T. Muscular Dystrophy Therapy by Non-autologous Mesenchymal Stem Cells: Muscle Regeneration without Immunosuppression and Inflammation. *Transplantation* **2009**, *87*, 1275.
8. Montarras, D.; Morgan, J.; Collins, C.; Relaix, F.; Zaffran, S.; Cumano, A.; Partridge, T.; Buckingham, M. Direct Isolation of Satellite Cells for Skeletal Muscle Regeneration. *Science* **2005**, *309*, 2064.
9. Markert, C. D.; Atala, A.; Cann, J. K.; Christ, G.; Furth, M.; Ambrosio, F.; Childers, M. K. Mesenchymal Stem Cells: Emerging Therapy for Duchenne Muscular Dystrophy. *PM&R* **2009**, *1*, 547–559.
10. Liechty, K. W.; MacKenzie, T. C.; Shaaban, A. F.; Radu, A.; Moseley, A.; Deans, R.; Marshak, D. R.; Flake, A. W. Human Mesenchymal Stem Cells Engraft and Demonstrate Site-Specific Differentiation after *in Utero* Transplantation in Sheep. *Nat. Med.* **2000**, *6*, 1282–1286.
11. Ichim, T. E.; Alexandrescu, D. T.; Solano, F.; Lara, F.; Campion, R. D. N.; Paris, E.; Woods, E. J.; Murphy, M. P.; Dasanu, C. A.; Patel, A. N. Mesenchymal Stem Cells as Anti-inflammatories: Implications for Treatment of Duchenne Muscular Dystrophy. *Cell. Immunol.* **2010**, *260*, 75–82.
12. Krampera, M.; Pizzolo, G.; Aprili, G.; Franchini, M. Mesenchymal Stem Cells for Bone, Cartilage, Tendon and Skeletal Muscle Repair. *Bone* **2006**, *39*, 678–683.
13. Jiang, Y.; Jahagirdar, B. N.; Reinhardt, R. L.; Schwartz, R. E.; Keene, C. D.; Ortiz-Gonzalez, X. R.; Reyes, M.; Lenvik, T.; Lund, T.; Blackstad, M. Pluripotency of Mesenchymal Stem Cells Derived from Adult Marrow. *Nature* **2002**, *418*, 41–49.
14. Segers, V. F.; Lee, R. T. Stem-Cell Therapy for Cardiac Disease. *Nature* **2008**, *451*, 937–942.
15. de Vries, I. J.; Lesterhuis, W. J.; Barentsz, J. O.; Verdijk, P.; van Krieken, J. H.; Boerman, O. C.; Oyen, W. J.; Bonenkamp, J. J.; Boezeman, J. B.; Adema, G. J.; *et al.* Magnetic Resonance Tracking of Dendritic Cells in Melanoma Patients for Monitoring of Cellular Therapy. *Nat. Biotechnol.* **2005**, *23*, 1407–1413.
16. Bulte, J. W. M. *In Vivo* MRI Cell Tracking: Clinical Studies. *Am. J. Roentgen.* **2009**, *193*, 314–325.
17. Kircher, M. F.; Gambhir, S. S.; Grimm, J. Noninvasive Cell-Tracking Methods. *Nat. Rev. Clin. Pract.* **2011**, *8*, 677–688.
18. Modo, M.; Cash, D.; Mellodew, K.; Williams, S. C. R.; Fraser, S. E.; Meade, T. J.; Price, J.; Hodges, H. Tracking Transplanted Stem Cell Migration Using Bifunctional, Contrast Agent-Enhanced, Magnetic Resonance Imaging. *Neuroimage* **2002**, *17*, 803–811.
19. Kraitchman, D. L.; Heldman, A. W.; Atalar, E.; Amado, L. C.; Martin, B. J.; Pittenger, M. F.; Hare, J. M.; Bulte, J. W. M. *In Vivo* Magnetic Resonance Imaging of Mesenchymal Stem Cells in Myocardial Infarction. *Circulation* **2003**, *107*, 2290–2293.
20. Hill, J. M.; Dick, A. J.; Raman, V. K.; Thompson, R. B.; Yu, Z. X.; Hinds, K. A.; Pessanha, B. S. S.; Guttman, M. A.; Varney, T. R.; Martin, B. J. Serial Cardiac Magnetic Resonance Imaging of Injected Mesenchymal Stem Cells. *Circulation* **2003**, *108*, 1009–1014.
21. Foster Gareau, P.; Heyn, C.; Alejski, A.; Rutt, B. K. Imaging Single Mammalian Cells with a 1.5 T Clinical MRI Scanner. *Magn. Reson. Med.* **2003**, *49*, 968–971.
22. Shapiro, E. M.; Sharer, K.; Skrtic, S.; Koretsky, A. P. *In Vivo* Detection of Single Cells by MRI. *Magn. Reson. Med.* **2006**, *55*, 242–249.
23. Xu, M.; Wang, L. V. Photoacoustic Imaging in Biomedicine. *Rev. Sci. Instrum.* **2006**, *77*, 041101−1–041101−22.
24. Razansky, D.; Distel, M.; Vinegoni, C.; Ma, R.; Perrimon, N.; Koster, R. W.; Ntziachristos, V. Multispectral Opto-Acoustic Tomography of Deep-Seated Fluorescent Proteins *in Vivo*. *Nat. Photon.* **2009**, *3*, 412–417.
25. Zerda, A.; Liu, Z.; Bodapati, S.; Teed, R.; Vaithilingam, S.; Khuri-Yakub, B. T.; Chen, X.; Dai, H.; Gambhir, S. S. Ultrahigh Sensitivity Carbon Nanotube Agents for Photoacoustic Molecular Imaging in Living Mice. *Nano Lett.* **2010**, *10*, 2168–2172.
26. Razansky, D.; Vinegoni, C.; Ntziachristos, V. Multispectral Photoacoustic Imaging of Fluorochromes in Small Animals. *Opt. Lett.* **2007**, *32*, 2891–2893.
27. Kostli, K. P.; Beard, P. C. Two-Dimensional Photoacoustic Imaging by Use of Fourier-Transform Image Reconstruction and a Detector with an Anisotropic Response. *Appl. Opt.* **2003**, *42*, 1899–1908.
28. Kim, J. W.; Galanzha, E. I.; Shashkov, E. V.; Moon, H. M.; Zharov, V. P. Golden Carbon Nanotubes as Multimodal Photoacoustic and Photothermal High-Contrast Molecular Agents. *Nat. Nanotechnol.* **2009**, *4*, 688–694.

29. Lu, W.; Huang, Q.; Ku, G.; Wen, X.; Zhou, M.; Guzatov, D.; Brecht, P.; Su, R.; Oraevsky, A.; Wang, L. V. Photoacoustic Imaging of Living Mouse Brain Vasculature Using Hollow Gold Nanospheres. *Biomaterials* **2010**, *31*, 2617–2626.

30. Kruger, R. A.; Lam, R. B.; Reinecke, D. R.; Del Rio, S. P.; Doyle, R. P. Photoacoustic Angiography of the Breast. *Med. Phys* **2010**, *37*, 6096–6100.

31. Wang, X.; Xie, X.; Ku, G.; Wang, L. V.; Stoica, G. Noninvasive Imaging of Hemoglobin Concentration and Oxygenation in The Rat Brain Using High-Resolution Photoacoustic Tomography. *J. Biomed. Opt.* **2006**, *11*, 024015−1– 024015−9.

32. Levi, J.; Kothapalli, S. R.; Ma, T. J.; Hartman, K.; Khuri-Yakub, B. T.; Gambhir, S. S. Design, Synthesis, and Imaging of an Activatable Photoacoustic Probe. *J. Am. Chem. Soc.* **2010**, *132*, 11264–11269.

33. De la Zerda, A.; Zavaleta, C.; Keren, S.; Vaithilingam, S.; Bodapati, S.; Liu, Z.; Levi, J.; Smith Bryan, R.; Ma, T.-J.; Oralkan, O.; Khuri-Yakub Butrus, T.; Gambhir Sanjiv, S.; *et al.* Carbon Nanotubes as Photoacoustic Molecular Imaging Agents in Living Mice. *Nat. Nanotechnol.* **2008**, *3*, 557–562.

34. Tong, L.; Wei, Q.; Wei, A.; Cheng, J. X. Gold Nanorods as Contrast Agents for Biological Imaging: Optical Properties, Surface Conjugation and Photothermal Effects. *Photochem. Photobiol.* **2009**, *85*, 21–32.

35. Chen, Y. S.; Frey, W.; Kim, S.; Kruizinga, P.; Homan, K.; Emelianov, S. Silica-Coated Gold Nanorods as Photoacoustic Signal Nanoamplifiers. *Nano Lett.* **2011**, *11*, 348–354.

36. Slowing, I.; Trewyn, B. G.; Victor, S. Y. L. Effect of Surface Functionalization of MCM-41-Type Mesoporous Silica Nanoparticles on The Endocytosis by Human Cancer Cells. *J. Am. Chem. Soc.* **2006**, *128*, 14792–14793.

37. Chen, L. C.; Wei, C. W.; Souris, J. S.; Cheng, S. H.; Chen, C. T.; Yang, C. S.; Li, P. C.; Lo, L. W. Enhanced Photoacoustic Stability of Gold Nanorods by Silica Matrix Confinement. *J. Biomed. Opt.* **2010**, *15*, 016010.

38. Hackley, V. A.; Clogston, J. D. Measuring The Hydrodynamic Size of Nanoparticles in Aqueous Media Using Batch-Mode Dynamic Light Scattering. *Methods Mol. Biol.* **2011**, *697*, 35–52.

39. Labbaf, S.; Tsigkou, O.; Muller, K. H.; Stevens, M. M.; Porter, A. E.; Jones, J. R. Spherical Bioactive Glass Particles and Their Interaction with Human Mesenchymal Stem Cells *in vitro*. *Biomaterials* **2010**, *32*, 1010–1018.

40. Chung, T. H.; Wu, S. H.; Yao, M.; Lu, C. W.; Lin, Y. S.; Hung, Y.; Mou, C. Y.; Chen, Y. C.; Huang, D. M. The Effect of Surface Charge on The Uptake and Biological Function of Mesoporous Silica Nanoparticles in 3T3-L1 Cells and Human Mesenchymal Stem Cells. *Biomaterials* **2007**, *28*, 2959–2966.

41. Jokerst, J. V.; Miao, Z.; Zavaleta, C.; Cheng, Z.; Gambhir, S. S. Affibody-Functionalized Gold-Silica Nanoparticles for Raman Molecular Imaging of The Epidermal Growth Factor Receptor. *Small* **2011**, *7*, 625–633.

42. Ricles, L. M.; Nam, S. Y.; Sokolov, K.; Emelianov, S. Y.; Suggs, L. J. Function of Mesenchymal Stem Cells Following Loading of Gold Nanotracers. *Int. J. Nanomed.* **2011**, *6*, 407–416.

43. Hsiao, J. K.; Tsai, C. P.; Chung, T. H.; Hung, Y.; Yao, M.; Liu, H. M.; Mou, C. Y.; Yang, C. S.; Chen, Y. C.; Huang, D. M. Mesoporous Silica Nanoparticles as a Delivery System of Gadolinium for Effective Human Stem Cell Tracking. *Small* **2008**, *4*, 1445–1452.

44. Amaral, M.; Costa, M.; Lopes, M.; Silva, R.; Santos, J.; Fernandes, M. Si$_3$N$_4$-Bioglass Composites Stimulate The Proliferation of Mg63 Osteoblast-like Cells and Support The Osteogenic Differentiation of Human Bone Marrow Cells. *Biomaterials* **2002**, *23*, 4897–4906.

45. Aggarwal, S.; Pittenger, M. F. Human Mesenchymal Stem Cells Modulate Allogeneic Immune Cell Responses. *Blood* **2005**, *105*, 1815–1822.

46. Dunbar, S. A. Applications of Luminex Xmap Technology for Rapid, High-Throughput Multiplexed Nucleic Acid Detection. *Clin. Chim. Acta* **2006**, *363*, 71–82.

47. Chen, L. C.; Wei, C. W.; Souris, J. S.; Cheng, S. H.; Chen, C. T.; Yang, C. S.; Li, P. C.; Lo, L. W. Enhanced Photoacoustic Stability of Gold Nanorods by Silica Matrix Confinement. *J. Biomed. Opt.* **2010**, *15*, 016010−1–016010−6.

48. Sampaolesi, M.; Blot, S.; D'Antona, G.; Granger, N.; Tonlorenzi, R.; Innocenzi, A.; Mognol, P.; Thibaud, J. L.; Galvez, B. G.; Barthelemy, I. Mesoangioblast Stem Cells Ameliorate Muscle Function in Dystrophic Dogs. *Nature* **2006**, *444*, 574–579.

49. Li, P. C.; Wei, C. W.; Liao, C. K.; Chen, C. D.; Pao, K. C.; Wang, C. R. C.; Wu, Y. N.; Shieh, D. B. Photoacoustic Imaging of Multiple Targets Using Gold Nanorods. *IEEE Ultrason. Ferroelec. Freq.* **2007**, *54*, 1642–1647.

50. Hauck, T. S.; Ghazani, A. A.; Chan, W. C. W. Assessing The Effect of Surface Chemistry on Gold Nanorod Uptake, Toxicity, and Gene Expression in Mammalian Cells. *Small* **2008**, *4*, 153–159.

51. Alkilany, A. M.; Nagaria, P. K.; Hexel, C. R.; Shaw, T. J.; Murphy, C. J.; Wyatt, M. D. Cellular Uptake and Cytotoxicity of Gold Nanorods: Molecular Origin of Cytotoxicity and Surface Effects. *Small* **2009**, *5*, 701–708.

52. Gonzalez McQuire, R.; Green, D. W.; Partridge, K. A.; Oreffo, R. O. C.; Mann, S.; Davis, S. A. Coating of Human Mesenchymal Cells in 3D Culture with Bioinorganic Nanoparticles Promotes Osteoblastic Differentiation and Gene Transfection. *Adv. Mater.* **2007**, *19*, 2236–2240.

53. Huang, D. M.; Chung, T. H.; Hung, Y.; Lu, F.; Wu, S. H.; Mou, C. Y.; Yao, M.; Chen, Y. C. Internalization of Mesoporous Silica Nanoparticles Induces Transient but Not Sufficient Osteogenic Signals in Human Mesenchymal Stem Cells. *Toxicol. Appl. Pharmacol.* **2008**, *231*, 208–215.

54. Discher, D. E.; Mooney, D. J.; Zandstra, P. W. Growth Factors, Matrices, and Forces Combine and Control Stem Cells. *Science* **2009**, *324*, 1673–1677.

55. Didychuk, C. L.; Ephrat, P.; Chamson-Reig, A.; Jacques, S. L.; Carson, J. J. L. Depth of Photothermal Conversion of Gold Nanorods Embedded in a Tissue-like Phantom. *Nanotechnology* **2009**, *20*, 195102.

56. Nikoobakht, B.; El-Sayed, M. Preparation and Growth Mechanism of Gold Nanorods (NRs) Using Seed-Mediated Growth Method. *Chem. Mater.* **2003**, *15*, 1957–1962.

57. Wei, A.; Leonov, A. P.; Wei, Q. Gold Nanorods: Multifunctional Agents for Cancer Imaging and Therapy. *Methods Mol. Biol.* **2010**, *624*, 119–130.

58. Liao, H.; Hafner, J. H. Gold Nanorod Bioconjugates. *Chem. Mater.* **2005**, *17*, 4636–4641.

59. Orendorff, C. J.; Murphy, C. J. Quantitation of Metal Content in the Silver-Assisted Growth of Gold Nanorods. *J. Phys. Chem. B* **2006**, *110*, 3990–3994.

60. Gorelikov, I.; Matsuura, N. Single-Step Coating of Mesoporous Silica on Cetyltrimethyl Ammonium Bromide-Capped Nanoparticles. *Nano Lett.* **2008**, *8*, 369–373.

61. Craig-Schapiro, R.; Kuhn, M.; Xiong, C.; Pickering, E. H.; Liu, J.; Misko, T. P.; Perrin, R. J.; Bales, K. R.; Soares, H.; Fagan, A. M. Multiplexed Immunoassay Panel Identifies Novel CSF Biomarkers for Alzheimer's Disease Diagnosis and Prognosis. *PLoS One* **2011**, *6*, e18850.

62. Needles, A.; Heinmiller, A.; Ephrat, P.; Bilan-Tracey, C.; Trujillo, A.; Theodoropoulos, C.; Hirson, D.; Foster, F. In Development of a Combined Photoacoustic Micro-Ultrasound System for Estimating Blood Oxygenation. IEEE Ultrasonics Symposium, Oct 11−14, 2010, San Diego, CA; pp 390−393.

63. Thakor, A. S.; Paulmurugan, R.; Kempen, P.; Zavaleta, C.; Sinclair, R.; Massoud, T. F.; Gambhir, S. S. Oxidative Stress Mediates The Effects of Raman Active Gold Nanoparticles in Human Cells. *Small* **2011**, *7*, 126–136.

64. Abramoff, M. D.; Magalhaes, P. J.; Ram, S. J. Image Processing with ImageJ. *Biophoton. Intl.* **2004**, *11*, 36–42.